Hindawi
International Journal of Antennas and Propagation
Volume 2021, Article ID 5503330, 16 pages
https://doi.org/10.1155/2021/5503330

Research Article

Unsteady Aerodynamic Characteristics of Antenna Rotating in Different Elevation Angles

Yanqi Zhang and Zhaoming Zhang

Key Lab of Ministry of Industry and Information Technology for Unsteady Aerodynamics and Flow Control, College of Aerospace Engineering, Nanjing University of Aeronautics and Astronautics, Nanjing, Jiangsu 210016, China

Correspondence should be addressed to Yanqi Zhang; yanqizhang_nuaa@163.com

Received 19 April 2021; Accepted 13 July 2021; Published 27 July 2021

Academic Editor: Mohammad Alibakhshikenari

The aerodynamic characteristics of radar antennas should be considered in computing their wind resistance and designing pedestal servo systems. In this paper, the aerodynamic characteristics of a flat plate antenna with azimuthal rotation are explored using a wind tunnel, and the effects of the antenna elevation angle and reduced frequency on the aerodynamic coefficients are analyzed. The corresponding results of numerical simulation are given to compare with the experimental results. The variation of aerodynamic coefficients with respect to the azimuth angle is found to depend on the reduced frequency and the antenna elevation angle. When the increase in antenna elevation angle is slight, the mean and root mean square values of the aerodynamic coefficients are not monotonic with respect to increases in elevation angle and may increase at individual elevation angles. When the elevation angle increases significantly, the mean, maximum, and root mean square values of the aerodynamic coefficients all significantly decrease. The simulation results are in good agreement with the experimental results, which verify the feasibility of using unsteady numerical simulations to obtain the flow field structure when the antenna is rotating. This approach allows the influence mechanism of the elevation angle change on the aerodynamic characteristics of the rotating antenna to be identified.

1. Introduction

For the radar antenna working in the open air, wind load is the main source of its load. In recent years, there are many researches on the electrical performance of radar antenna [1], but with the increase in the volume and weight of radar antenna, the importance of antenna aerodynamic characteristics (aerodynamic coefficient, surface pressure coefficient) in its wind resistance performance design, structural strength check, and servo system design are gradually highlighted [2]. The influence of antenna attitude (e.g., elevation angle, azimuth angle) on the steady aerodynamic characteristics (e.g., aerodynamic coefficient and surface pressure distribution) of antenna has become the research focus of many scholars [3–5].

With the large-scale application of the radar antenna azimuth scanning method, there are strict restrictions on the gradient of the rotation angular velocity when the antenna is running [6]. Compared with the static antenna, the continuous rotation of the antenna causes it to be subject to the time-varying dynamic wind load. Excessive dynamic wind load will increase the fatigue damage of the antenna structure and decrease the scanning precision. Previously, in the structural design of radar antennas, designers mostly used the root mean square (rms) value of the steady aerodynamic coefficient when the antenna was at rest as the reference data for structural design.

In addition, most of the existing wind tunnel tests and numerical simulations focus on the steady aerodynamic characteristics of the antenna [7–10]. In the field of radar antenna study, there is lack of study on the influence of antenna elevation on the unsteady aerodynamic characteristics of the antenna in azimuth rotation, yet little study has been undertaken on the specific differences between the steady aerodynamic characteristics of the antenna in stationary rotation and the unsteady aerodynamic

characteristics of the antenna in azimuth rotation. Therefore, the difference between the two has become an urgent concern for designers. In order to solve this problem, Sachs [11] proposed a semiempirical formula to calculate and predict the dynamic azimuth torque of a rotating antenna by using the drag and azimuth moment of the antenna at rest. However, the application scope and accuracy of the formula are worthy of further study. Lombardi [12] pointed out, in his research through wind tunnel force test, that the semiempirical formula does not consider the influence of the lateral force on the dynamic azimuth moment of the radar antenna. In addition, Lombardi's experimental results show that the maximum drag coefficient when the antenna is rotating is about 30% higher than that when the antenna is stationary. Muggiasca et al. [13] also pointed out, in their research, that the peak torque of the motor driving the antenna in the rotation is significantly different from that in the static state. Gumusel et al. [14] studied the influence of rotating motion on the vibration and noise of antenna and considered that the aggravation of vibration and noise was caused by the antenna rotating motion cutting off the downstream propagation of the shedding vortex.

For the research on the unsteady aerodynamic characteristics of the antenna with azimuth rotation, on the one hand, the existing research objects are mostly focused on the drum type radar antenna. Although there are many types of radar antennas (e.g., flat plate, parabola, hyperboloid, hollow out, drum, etc.), flat plate is always the most classic shape structure of radar antenna. Therefore, the research on unsteady aerodynamic characteristics of flat plate antenna becomes extremely urgent [7, 8]. On the other hand, the existing research only studies the antenna drag, lift, and azimuth moment, while it is not adequate for the research on the lateral force, pitching moment, and the root mean square value of aerodynamic coefficient involved frequently. These are also important parameters in the structural design of antenna with azimuth rotation function.

Through the establishment of an antenna dynamic force test platform, wind tunnel dynamic force measurement tests were performed on flat antenna models at different elevation angles and reduced frequencies, and the unsteady aerodynamic characteristics of the antenna were obtained when the antenna rotated at different reduced frequencies compared to the elevation angle changes. Compared with the numerical simulation results, the feasibility of the numerical simulation method to study the unsteady aerodynamic characteristics of the antenna is verified. Therefore, the influence of the change of elevation angle on the distribution of the flow field around the rotating antenna is analyzed, so as to provide reference and basis for the design of the radar antenna with azimuth rotation.

2. Experimental Method

2.1. Wind Tunnel and Model. A radar antenna dynamic force measurement test was carried out in the NH-2 closed-loop low-speed wind tunnel at Nanjing University of Aeronautics and Astronautics. The size of the test section is (length × width × height) 3 m × 2.5 m × 6 m, the degree of turbulence can be varied from $\varepsilon \leq 0.10$–0.14%, and the maximum wind speed is 90 m/s, and the overall schematic diagram of the wind tunnel is shown in Figure 1(a). The antenna modal is a flat plate antenna, and the model consists of a support rod, an elevation angle adjustment mechanism, and an antenna array. The antenna array has a length of $L = 0.5$ m, a width of $W = 0.2$ m, a thickness of $C = 0.02$ m, and an antenna height of $H = 0.36$ m; it can adjust the elevation angle of $\alpha = 0^\circ$, 10°, 20°, and 30°, as shown in Figure 1(b). The field installation of the test model is depicted in Figure 1(c), and the shooting direction is assigned in the positive direction of the x-axis of the coordinate system.

2.2. Definition of the Coordinate System and Aerodynamic Parameters. The aerodynamic load acting on the model is measured in the body-axis system with a six-component box strain balance. The body-axis system is converted into a wind shaft system using a coordinate-transformation formula [15]. Finally, the aerodynamic load on the model is given in the wind-axis coordinate system. As shown in Figure 2, the reference position for the balance moment is point O, and the reference coordinate system for the force measurement test platform is OXYZ. In the wind-axis coordinate system, the three force components of strain balance are drag (F_x), lift (F_y), and lateral force (F_z); the three-moment components are the rolling moment (M_x), azimuth moment (M_y), and pitching moment (M_z). The flow direction and positive drag direction are opposite to the positive direction of the x-axis in the reference coordinate system. When the front of the array is vertical to the incoming stream, the antenna elevation (α) is defined as 0°, and the antenna elevation angle in Figure 2 is positive.

In the stage of radar design, the wind load must be tested and validated, in order for the stiffness and strength of the structure to meet the operational requirements, and the power of the selected servo motor meets the standard working requirements of driving the radar antenna. The drag and azimuth moment of the antenna is used to determine the power of the servo motor, and the lateral force and pitching moment of the antenna are used to determine the lateral and longitudinal wind load stability of the antenna.

The primary purpose for studying the unsteady aerodynamic characteristics of the rotating antenna is to provide a design basis for the mechanical analysis of the servo drive system and antenna pedestal. This study only discusses the aerodynamic coefficient components essential for the design load and stable operation for the servo system of a radar antenna, which are the drag coefficient C_x, lateral force coefficient C_z, azimuth moment coefficient C_{my}, and pitching moment coefficient C_{mz}. Because the aerodynamic load changes periodically as the antenna rotates, we only analyze the aerodynamic coefficient results over one rotation period ($\beta = 0$–360°).

Using the formula for calculating the aerodynamic coefficients, the drag coefficient C_x, lateral force coefficient C_z, azimuth moment coefficient C_{my}, and pitching moment coefficient C_{mz} in the wind-axis coordinate system are shown in formulas (1)~(4) [11].

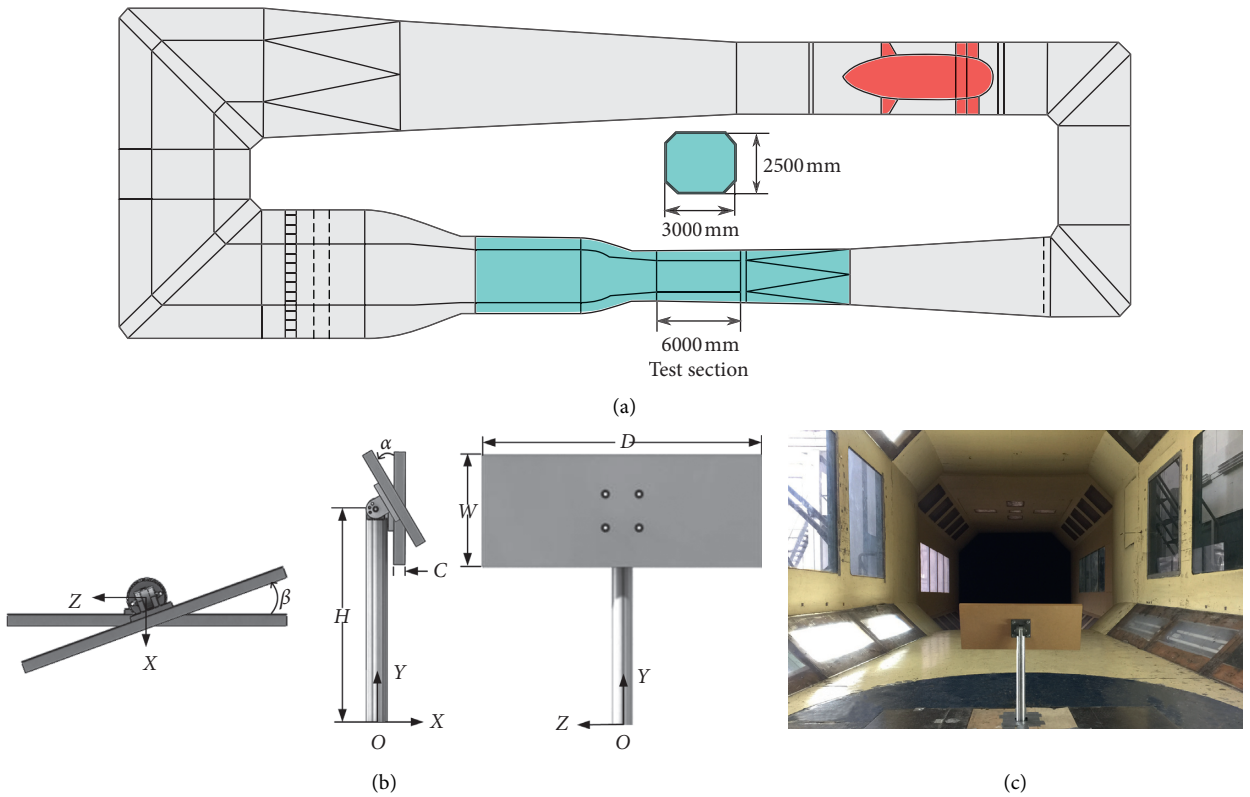

Figure 1: Radar antenna test model and wind tunnel test installation. (a) Overall schematic diagram of the wind tunnel (mm). (b) Schematic diagram of the radar antenna model ($\alpha = 0^\circ$, $\beta = 0^\circ$). (c) Wind tunnel test installation for the radar antenna model ($\alpha = 30^\circ$, $\beta = 0^\circ$).

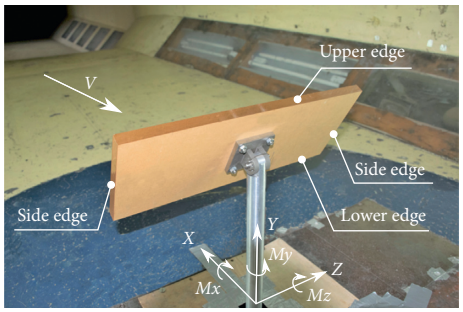

Figure 2: Definition of reference systems and aerodynamic parameters (wind-axis coordinate system).

$$C_x = \frac{F_x}{1/2\rho V^2 S}, \tag{1}$$

$$C_z = \frac{F_z}{1/2\rho V^2 S}, \tag{2}$$

$$C_{my} = \frac{M_y}{1/2\rho V^2 SL}, \tag{3}$$

$$C_{mz} = \frac{M_z}{1/2\rho V^2 SL}, \tag{4}$$

where ρ is the air density, V is the wind speed, L is the reference length ($L = 0.5$ m), and S is the model reference area ($S = L \times W = 0.1$ m^2).

2.3. Dynamic Force Test Platform. The dynamic force test platform has three main components: antenna model part, servo drive part, and data acquisition and processing part, and the schematic diagram for the antenna dynamic force test platform is presented in Figure 3.

The antenna model part includes an antenna array, support rod, and elevation angle adjustment mechanism, which can adjust the elevation and ground height of the model. The servo drive part includes a servo motor, driver, encoder, motion control card, and computer with a motion control program, which can drive model rotation and set motion parameters. The data acquisition and processing part includes a six-component box strain balance, slip ring, signal amplifier, photoelectric switch, data acquisition card, and computer with a data acquisition and processing program. The antenna model is connected to the six-component box strain balance with a flange, and both are installed on the servo motor. This part provides real-time monitoring of the aerodynamic coefficient during the azimuthal motion of the radar antenna.

After the model rotation becomes stable in the wind tunnel test, a photoelectric switch fixed at $\beta = 0^\circ$, the data

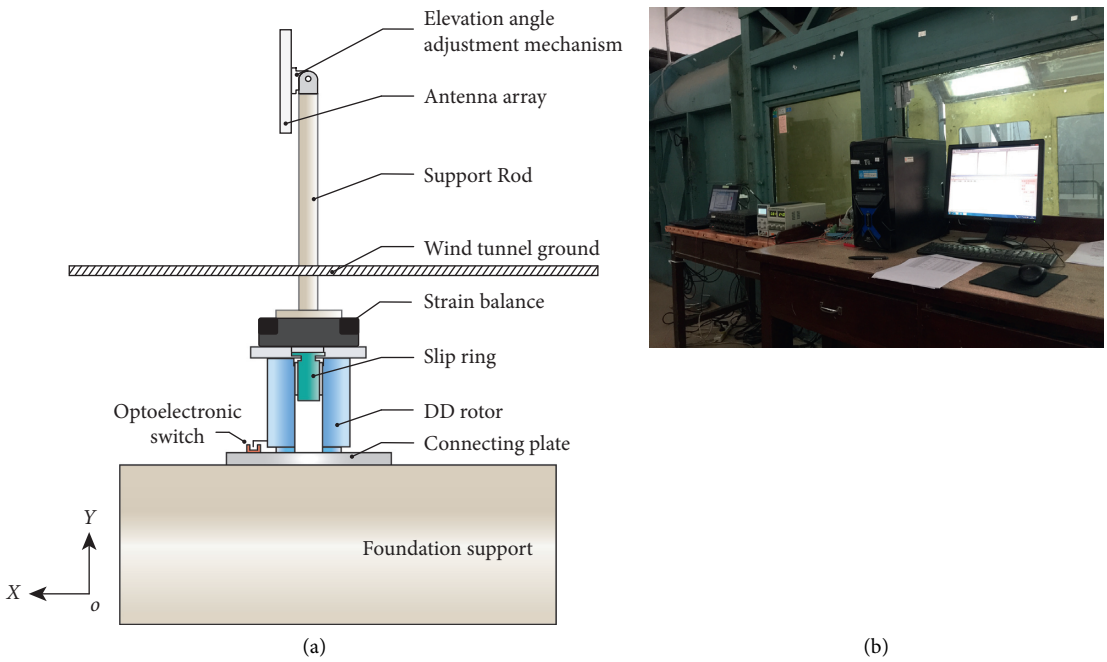

Figure 3: Schematic diagram of the dynamic force test platform, ($\alpha = 0^\circ$, $\beta = 0^\circ$). (a) Sectional view of test device. (b) Measurement and control system.

acquisition program will be triggered to collect the output signal for the balance. A "zero data set" is obtained before the wind tunnel is starting ($V = 0$ m/s) at each data point, and these data are deducted from the blowing data to consider the gravity and inertial forces of the antenna. The data obtained from the balance are mixed with the noise data generated by the vibration of the dynamic force test platform. In this study, a fourth-order Butterworth filter with a 5 Hz cutoff frequency is used to filter the original data, and zero phase filtering technology is adopted to avoid data lag caused by filtering [16]. The voltage signal is converted into the filtered unsteady aerodynamic coefficients using the balance formula and coordinate-conversion formula. The raw data and filtered data of the strain balance outputs in the wind-axis coordinate system, after deducting the "zero data set", are given in Figure 4. The figure indicates that this filtering method eliminates all high-frequency noise, and the filtered data follow the raw data well.

2.4. Test Parameters. The main similarity parameter for the rotating dynamic force measurement test for a radar antenna is the reduced frequency (K) [11], as shown in formula (5). In the design of the test, the influence of the periodic unsteady airflow inertial force is presented as a ratio of unsteady inertial force to steady airflow inertial force. This similarity parameter ensures that the velocity of each point in the flow field is proportional to that of the correspondence between the model and the real object, and the azimuth angles of corresponding velocity vectors are equal, allowing the test data to be directly applied to the real object.

$$K = \frac{N\ D}{V}, \tag{5}$$

where N is the angular velocity of the rotation (rad/s), D is the rotation diameter (m), $D = L$, and V is the wind velocity (m/s). In the wind tunnel tests, the inflow wind speed was set to $V = 15$ m/s, and the magnitude of the reduced frequency is varied by changing the angular velocity of rotation N. Tests at reduced frequencies of $K = 0.2$, 0.24, and 0.4 were conducted for the antenna, and its elevation angle was set to four values in turn: $\alpha = 0^\circ$, 10°, 20°, and 30°.

3. Experimental Results and Discussion

3.1. The Aerodynamic Coefficients of the Antenna Changes with Respect to Elevation Angle at Different Reduction Frequencies. When verifying the wind load stability of the antenna under the azimuthal rotation, the peak and peak-to-peak aerodynamic coefficients of the antenna are important reference indicators for the design of the antenna leveling system and wind resistance structure [13]. Figure 5 shows the change of aerodynamic coefficient with respect to the elevation angle at different reduced frequencies during a rotation period. C_x has positive peaks near $\beta = 180^\circ$ and 360°, and negative peaks near $\beta = 90^\circ$ and 270°. The difference of drag coefficient among different elevation angles mainly occurs in the azimuth area corresponding to the maximum windward area of the antenna, that is, near $\beta = 0^\circ$ and 180°, where the flow separation on the antenna surface is serious [17].

The change of C_x relative elevation angle will be affected by reduced frequency. As the reduced frequency increases, the peak-to-peak value of C_x will increase significantly. When $K = 0.2$, the positive peak of C_x decreases with an increase in elevation angle, and the peak-to-peak values of C_x are not significant among different elevation angles. When

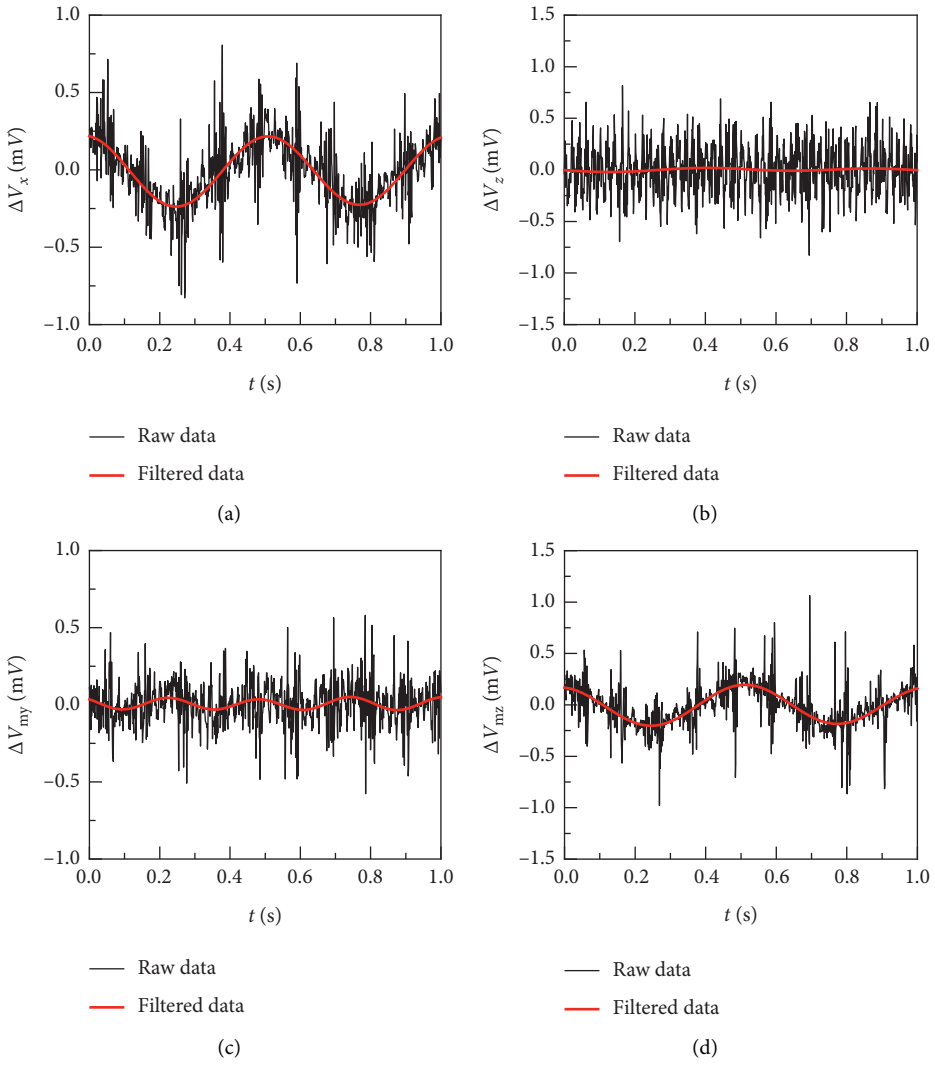

FIGURE 4: Raw and filtered data for the electrical signal output from the balance ($\alpha = 0^\circ$, $K = 0.4$, $t = 1$ s). (a) ΔV_x–t. (b) ΔV_z–t. (c) ΔV_{my}–t. (d) ΔV_{mz}–t.

$K = 0.24$, the peak value of C_x first increases and then decreases with respect to the elevation angle, and the azimuth angle corresponding to the peak value is advanced. When $K = 0.4$, the difference of the peak-to-peak value of C_x among different elevation angles increases significantly and is inversely proportional to the elevation angle. Besides, at the reduced frequencies of 0.2, 0.24, and 0.4, the maximum value of drag coefficient peak appears at elevation angles of 0°, 10°, and 0°, respectively. When the antenna rotates in azimuth at a largely reduced frequency, the sensitivity of peak and peak-to-peak of C_x to the elevation angle will increase; on the contrary, if the antenna is operated at a minor reduced frequency, the sensitivity of peak and peak-to-peak of C_x will decrease with increasing elevation angle.

The positive peaks of C_z appear near $\beta = 45^\circ$ and 215°, and the negative peak of C_z appears near $\beta = 135^\circ$ and 315°. Increasing the elevation angle will cause the peak advance or lag of the azimuth angle corresponding to the peak value. When $K = 0.2$, 0.24, and 0.4, the maximum value of lateral coefficient peaks appears at elevation angles of 10°, 0°, and 0°, respectively. Indeed, the change of C_z with azimuth is significantly affected by elevation angle. Compared with $\alpha = 0^\circ$, when $\alpha = 30^\circ$, the peak and peak-to-peak value of C_z decrease significantly. When the elevation angle is large, the peak-to-peak value of C_z is inversely proportional to the elevation angle and the reduced frequency.

The positive peaks of C_{my} appear at $\beta = 135^\circ$ and 315°, and the negative peak of C_{my} appears near $\beta = 45^\circ$ and 215°. Increasing the elevation angle will make the peak advance or lag at the azimuth angle corresponding to the peak value. The maximum value of azimuth moment coefficient peaks appeared at elevation angles of 10°, 0°, and 20°, respectively, at $K = 0.2$, 0.24, and 0.4. In addition, when $\alpha = 30^\circ$, the peak-to-peak value of C_{my} is the smallest, and it is irrelevant to the change of the reduced frequency. Note that the peak and peak-to-peak values of the azimuth moment coefficient decrease when $\alpha = 30^\circ$, and the peak-to-peak value is smaller in a rotation period.

The positive peaks of C_{mz} appear near $\beta = 90^\circ$ and 270°, and the negative peaks of C_{mz} appear near $\beta = 180^\circ$ and 360°.

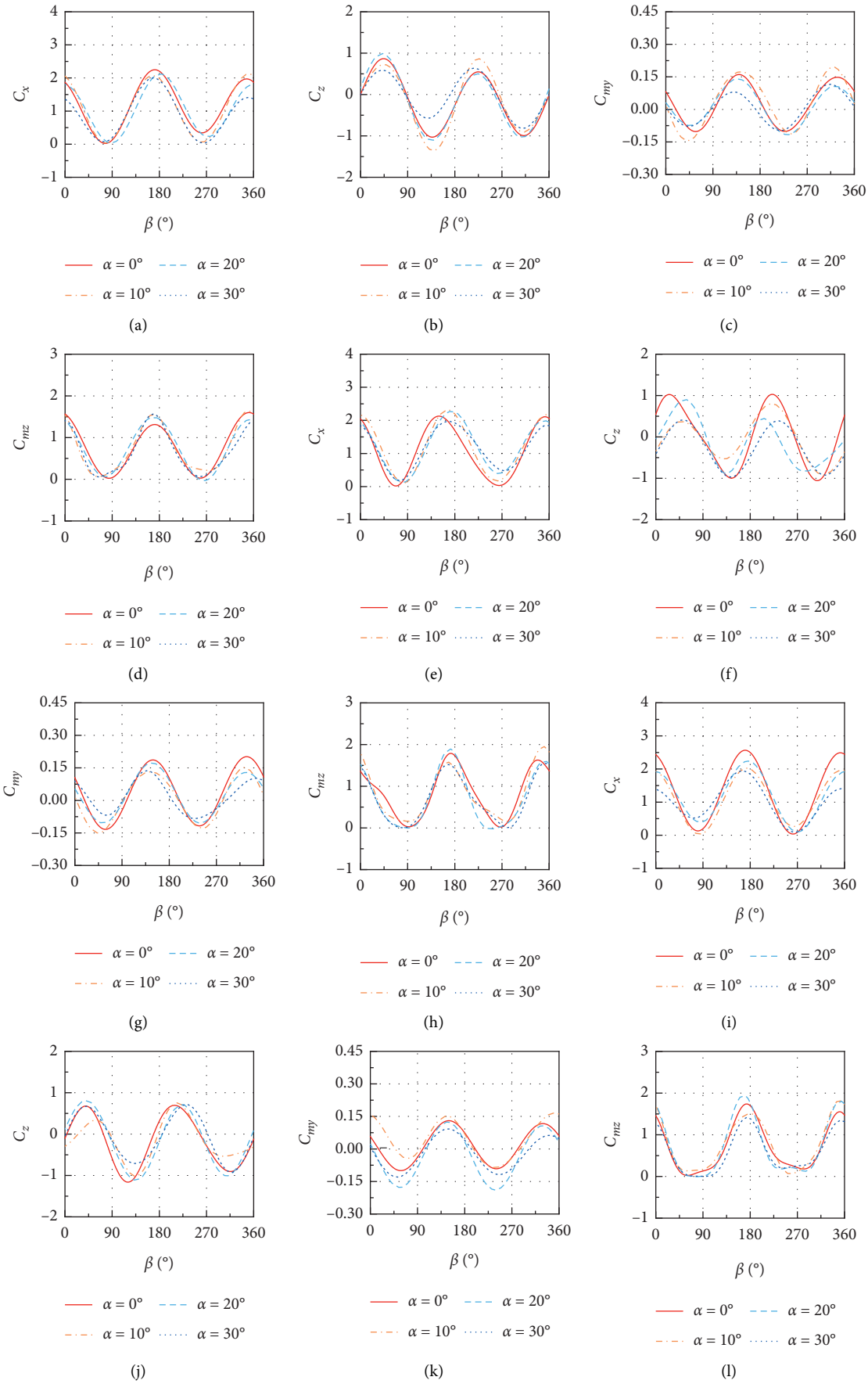

Figure 5: In one rotation period, aerodynamic coefficient with respect to elevation angle and reduced frequency. $\alpha = 0$–30°, $\Delta = 10^{\circ}$; (a)–(d): $K = 0.2$, (e)–(h): $K = 0.24$, (i)–(l): $K = 0.4$.

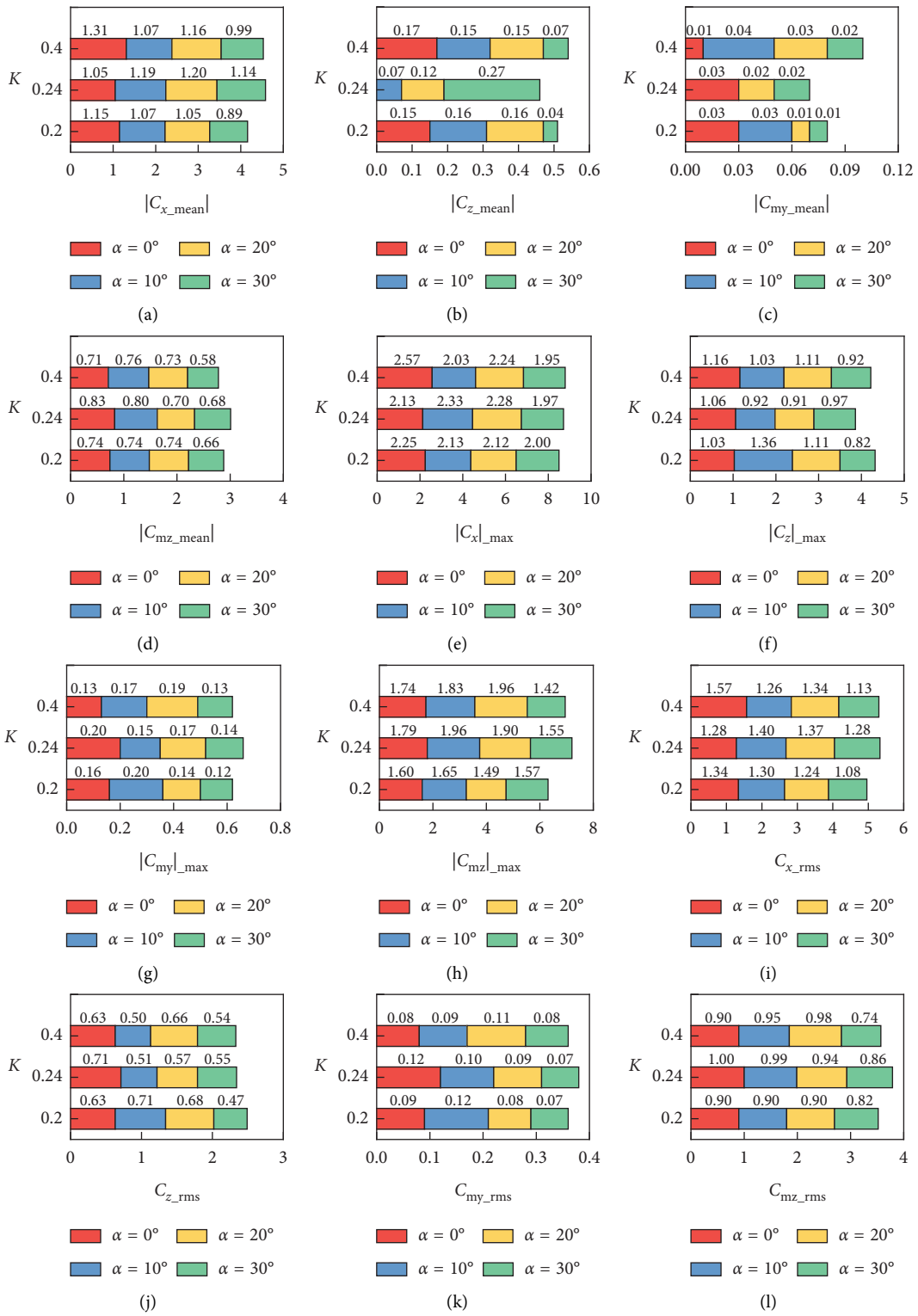

FIGURE 6: In one rotation period, mean, maximum, and root mean square values of the aerodynamic coefficients with respect to elevation angle and reduced frequency: $\alpha = 0$–30°, $K = 0.2$, 0.24, and 0.4. (a–d) Mean value; (e–h) maximum value; (i–l) root mean square value.

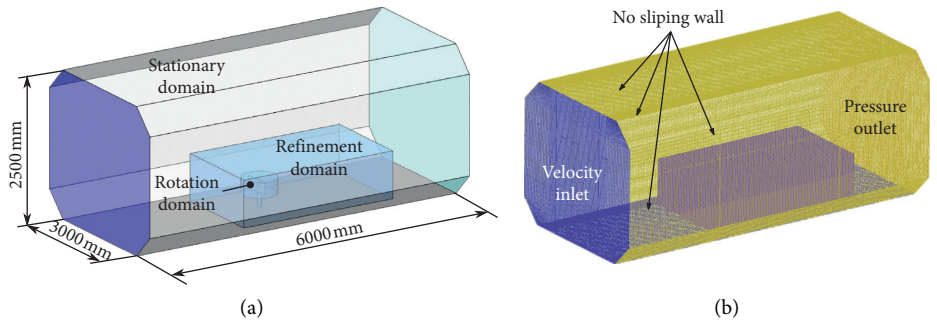

Figure 7: Numerical simulation of the computing domain for the wind tunnel and the grid division (perspective view). (a) Numerical simulation of the computing domain for the wind tunnel. (b) Grid division of the computing domain.

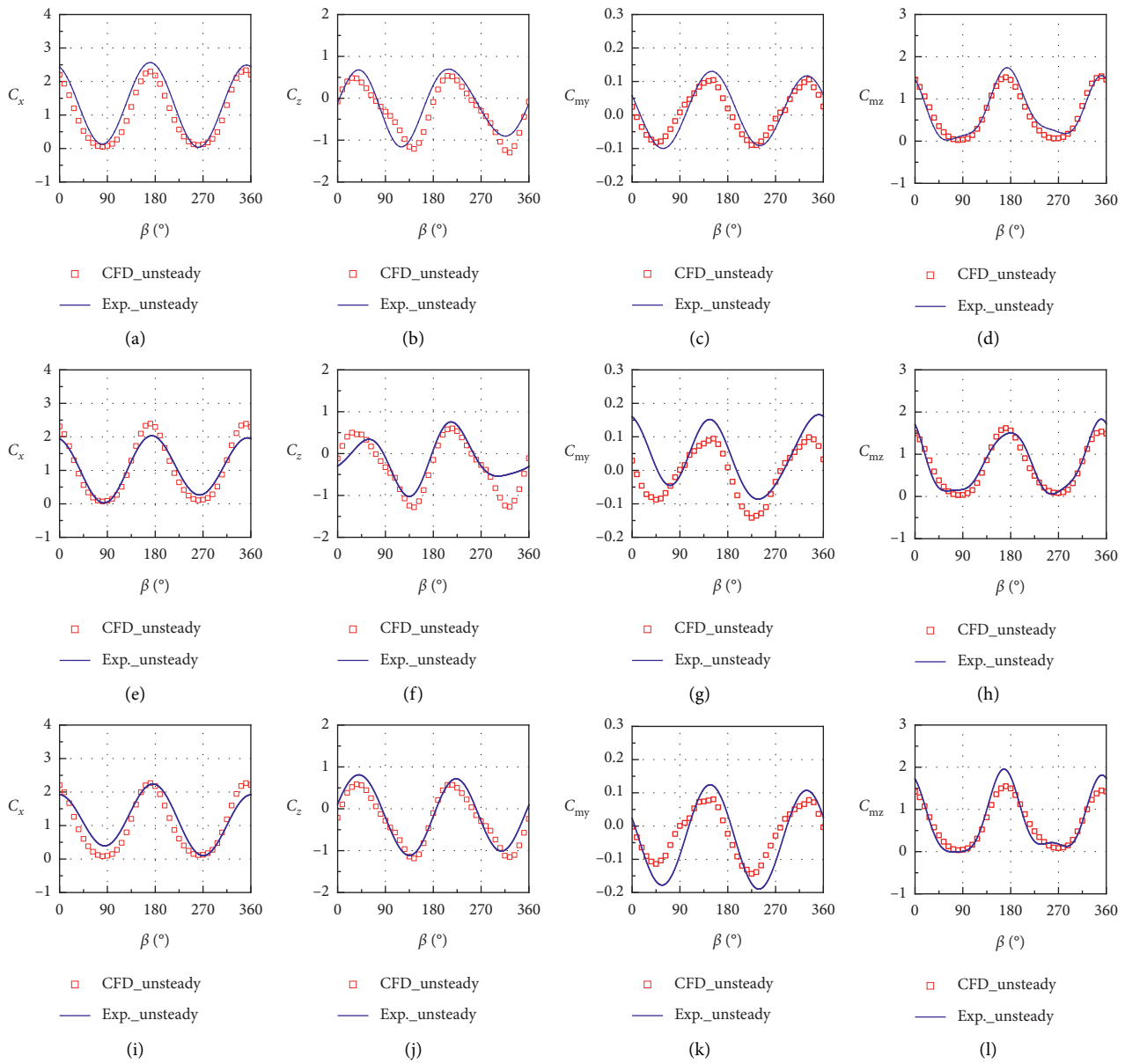

Figure 8: Continued.

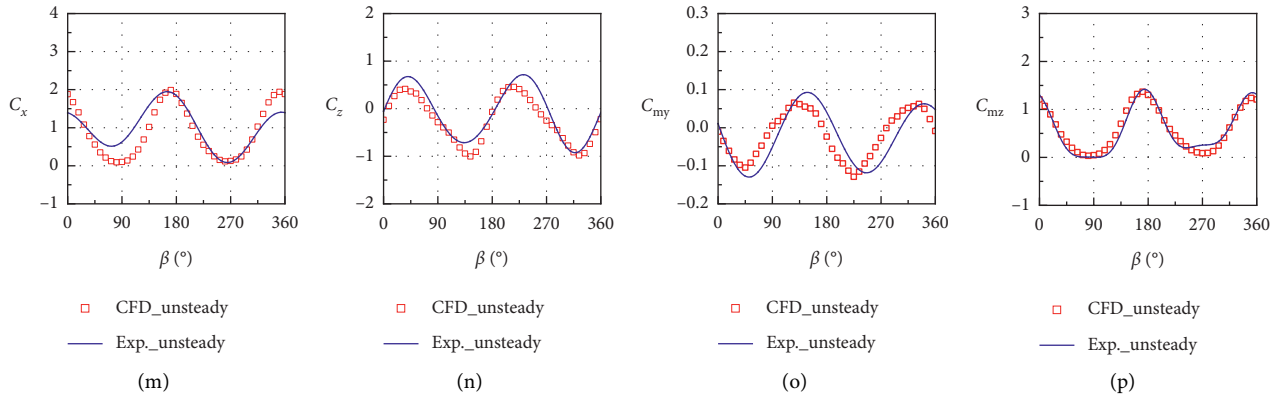

FIGURE 8: Test and simulation results of unsteady aerodynamic coefficients with respect to azimuth angle, $K = 0.4$. (a)–(d): $\alpha = 0^{\circ}$, (b)–(h): $\alpha = 10^{\circ}$, (i)–(l): $\alpha = 20^{\circ}$, (m)–(p): $\alpha = 30^{\circ}$.

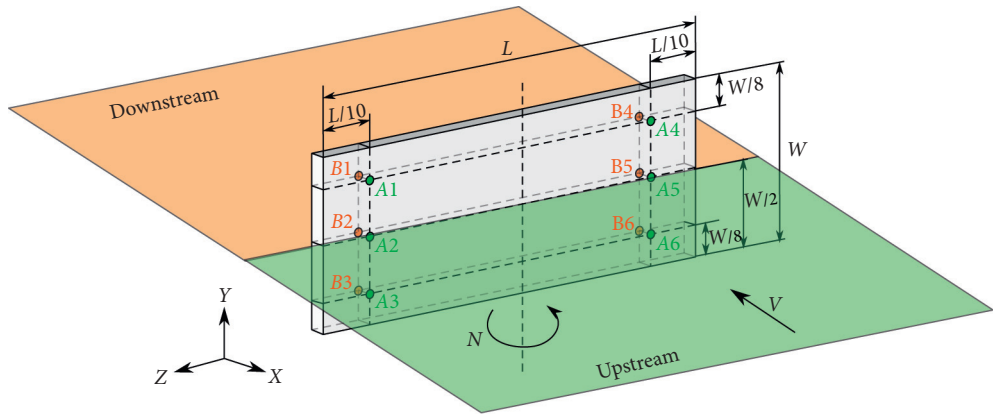

FIGURE 9: Pressure monitoring points on the surface of a flat plate antenna. The green region represents the antenna upstream, and the orange region represents the antenna downstream, counterclockwise rotation.

Obviously, an increase in the elevation angle does not make the azimuth angle corresponding to the peak advance or lag. When $K = 0.2$, 0.24, and 0.4, the maximum value of pitching moment peaks appears at the elevation angle of 10°, 10°, and 20°, respectively. It is worth noting that the change of C_{mz} is slower than that of azimuth angle at $\beta = 90^{\circ}$ and 270°, and this phenomenon becomes more evident with an increase in reduced frequency, but it is not sensitive to the elevation angle.

Increasing the elevation angle does not necessarily reduce the peak or peak-to-peak values of the aerodynamic coefficient, and the effect of reduced frequency should also be considered. At the same reduced frequency, the change of peak or peak-to-peak values of aerodynamic coefficient compared with the elevation angle does not show monotonicity. In addition, the peak-to-peak value of C_x, C_z, and C_{my} is the smallest at $\alpha = 30^{\circ}$ at different reduced frequencies. This indicates that a larger elevation angle can reduce the peak-to-peak values of aerodynamic coefficients to a certain extent compared with reduced frequencies.

3.2. Influence of Antenna Elevation Angle on the Mean, Maximum, and Root Mean Square Value of Aerodynamic Coefficients at Different Reduced Frequencies. The mean, maximum, and root mean square values of the aerodynamic coefficient for the antenna are important design references when designing the antenna pedestal. Figure 6 shows the mean, maximum, and root mean square values of aerodynamic coefficients with respect to the elevation angle in a rotation period, where $\alpha = 0$–30°, $K = 0.2$, 0.24, and 0.4 from Figures 6(a), 6(e), and 6(i), when $K = 0.24$ and $K = 0.4$, $|C_{x\_mean}|$, $|C_x|_{\_max}$ and C_{x_rms} have little change with respect to the reduced frequency and elevation angle, but when $K = 0.2$, they are affected by the elevation angle. When $K = 0.2$, $|C_{x\_mean}|$, $|C_x|_{\_max}$ and C_{x_rms} value is generally small. At different elevation angles, $|C_x|_{\_max}$ and C_{x_rms} have a minimum value when $\alpha = 30^{\circ}$, but the elevation angle increases from 0° to 30°. $|C_{x\_max}|$ and C_{x_rms} do not show a monotonic decreasing trend, especially $K = 0.24$, $\alpha = 10^{\circ}$.

From Figures 6(b), 6(f), and 6(j), $|C_{z\_mean}|$ changes significantly with respect to elevation angle and reduced frequency and increases with an increase in elevation angle and reduced frequency; that is, $|C_{z\_mean}|$ is sensitive to the change of reduced frequency and elevation angle. At the same reduced frequency, as the elevation angle increases, $|C_z|_{\_max}$ and C_{z_rms} do not show significant fluctuations, but compared with the reduced frequency, $|C_z|_{\_max}$ and C_{z_rms}

are less affected by the elevation angle. It should be noted that when $K = 0.42$, $|C_{z\_mean}|$, $|C_z|_{\_max}$ and C_{z_rms} are least affected by the elevation angle.

From Figures 6(c), 6(g), and 6(k), $|C_{my\_mean}|$ is more sensitive to the change of the reduced frequency and elevation angle. When $K = 0.4$ and $\alpha = 10^\circ$, $|C_{my\_mean}|$ is significantly greater than the results at other elevation angles. Moreover, $|C_{my}|_{\_max}$ and C_{my_rms} also showed higher sensitivity to the change of reduced frequency and elevation angle. When $K = 0.2$ and $\alpha = 10^\circ$, $|C_{my}|_{\_max}$ and C_{my_rms} results are largest; when $K = 0.24$ and $\alpha = 0^\circ$, $|C_{my}|_{\_max}$ and C_{my_rms} results are the largest; when $K = 0.4$ and $\alpha = 20^\circ$, $|C_{my}|_{\_max}$ and C_{my_rms} have the largest results. At three reduced frequencies, $|C_{my}|_{\_max}$ and C_{my_rms} are both the minimum when the elevation angle $\alpha = 30^\circ$.

From Figures 6(d), 6(h), and 6(l), during the antenna rotation at $K = 0.24$, changing the elevation angle cannot make $|C_{mz\_mean}|$, $|C_{mz}|_{\_max}$ and C_{mz_rms} decrease significantly. In addition, the minimum values of $|C_{mz\_mean}|$, $|C_{mz}|_{\_max,}$ and C_{mz_rms} all appear at $\alpha = 30^\circ$. Increasing the elevation angle can reduce $|C_{mz\_mean}|$, $|C_{mz}|_{\_max}$ and C_{mz_rms} to a certain extent, but it is not as significant as reduced frequency.

In summary, as the same reduced frequency, the mean, maximum, and root mean square values of the aerodynamic coefficient at $\alpha = 0$–30° do not show monotonicity compared with elevation. When the elevation angle is large, the mean, maximum, and root mean square value of the aerodynamic coefficient can be reduced to a certain extent, especially when $\alpha = 30^\circ$. It is not feasible for the azimuthal rotating antenna to reduce the mean value of the aerodynamic coefficient by a lower elevation angle. In contrast, a higher elevation angle can significantly reduce the maximum and root mean square value of the aerodynamic coefficient. Therefore, when obtaining the mean, maximum, and root mean square values of the aerodynamic coefficients under the azimuthal rotation of the antenna, the reduced frequency and the influence of the elevation angle need to be considered.

4. Verification of the Numerical Simulation Results

The unsteady numerical simulations obtain the unsteady flow field, as the antenna rotates in azimuth. The numerical simulation calculation domain was established according to the size of the wind tunnel test section, and the scale of the numerical simulation model is consistent with the wind tunnel test model. At the reduced frequency of $K = 0.4$, at $\alpha = 0^\circ$, 10°, 20°, and 30°, the flow field around the antenna is simulated when the antenna is rotated in azimuthal, and the numerical simulation results of the antenna aerodynamic coefficient are compared with the wind tunnel test results. The influence of elevation angle on the unsteady aerodynamic characteristics of the antenna and the correlation between unsteady flow and aerodynamic characteristics are also investigated.

Figure 7 shows the boundary conditions of the computational domain, and the results of grid generation in the computational domain cover a static domain, refinement domain, and rotational domain, from the outside to the inside, respectively. The static domain is divided by a structured mesh, whereas the refinement domain and the rotational domain are divided by an unstructured mesh. The surface of the antenna model is refined with an expansion-layer grid, with a total of approximately 8 million grid cells.

The shear-stress transport k-ω (SST k-ω) [18] turbulence model was used to simulate the unsteady flow field. The boundary for the velocity inlet was set to 15 m/s, the boundary for the pressure outlet was adopted, and the relative pressure was set to zero. Fixed-wall boundary conditions were used at the top, bottom, and side of the calculation domain. The aerodynamic coefficients of the antenna model in the wind-axis coordinate system were calculated and output.

Figure 8 shows the changes in aerodynamic coefficient wind tunnel test data and numerical simulation data with respect to the azimuth angle when $K = 0.4$, $\alpha = 0^\circ$, 10°, 20°, and 30°. The changing trends of the two are in good agreement, and the experimental result and the simulation result are slightly different in individual positions. The reason for this difference is that turbulence is an irregular flow of multiscale vortices. Compared with the direct numerical simulation, the contribution of small-scale vortices is absent in the simulation results after adding turbulence model [13, 19]. Wang et al. [20] also pointed out, in their research, that, for a flat plate with pitch motion, the local separation of small-scale vortices has a certain influence on the peak value of the aerodynamic coefficient. Therefore, the numerical simulation data are not completely consistent with the wind tunnel test data for the antenna in strong turbulence.

Although the turbulence model cannot accurately reproduce the vortex structure, especially the motion of different scale vortices, as the pressure distribution on the surface of the flat plate is related to the spatial structure of the large-scale vortex, and the small-scale vortices have little effect on the aerodynamic characteristics of the model [21, 22]. This further shows that the use of numerical simulation is feasible to analyze the correlation between the flow field distribution around the antenna and the unsteady aerodynamic characteristics. Indeed, Muggiasca et al. [13], Scarabino et al. [23], and Wu et al. [24] also reached a similar conclusion in their study.

4.1. The Wind Pressure Coefficient on the Antenna Surface Changes with Respect to the Elevation Angle. In the structural design of the antenna truss, the node position should be reasonably arranged according to the force, so that the position of the antenna surface with a more significant load is at the node of the truss, and the local stress on the wall is concentrated. In addition, in the finite element simulation analysis of the antenna antioverturning bracket, the time history curve of the wind pressure load on both sides of the antenna array is needed as the wind pressure load curve used in the finite element simulation. The following discusses the wind pressure coefficient changes at several antenna position

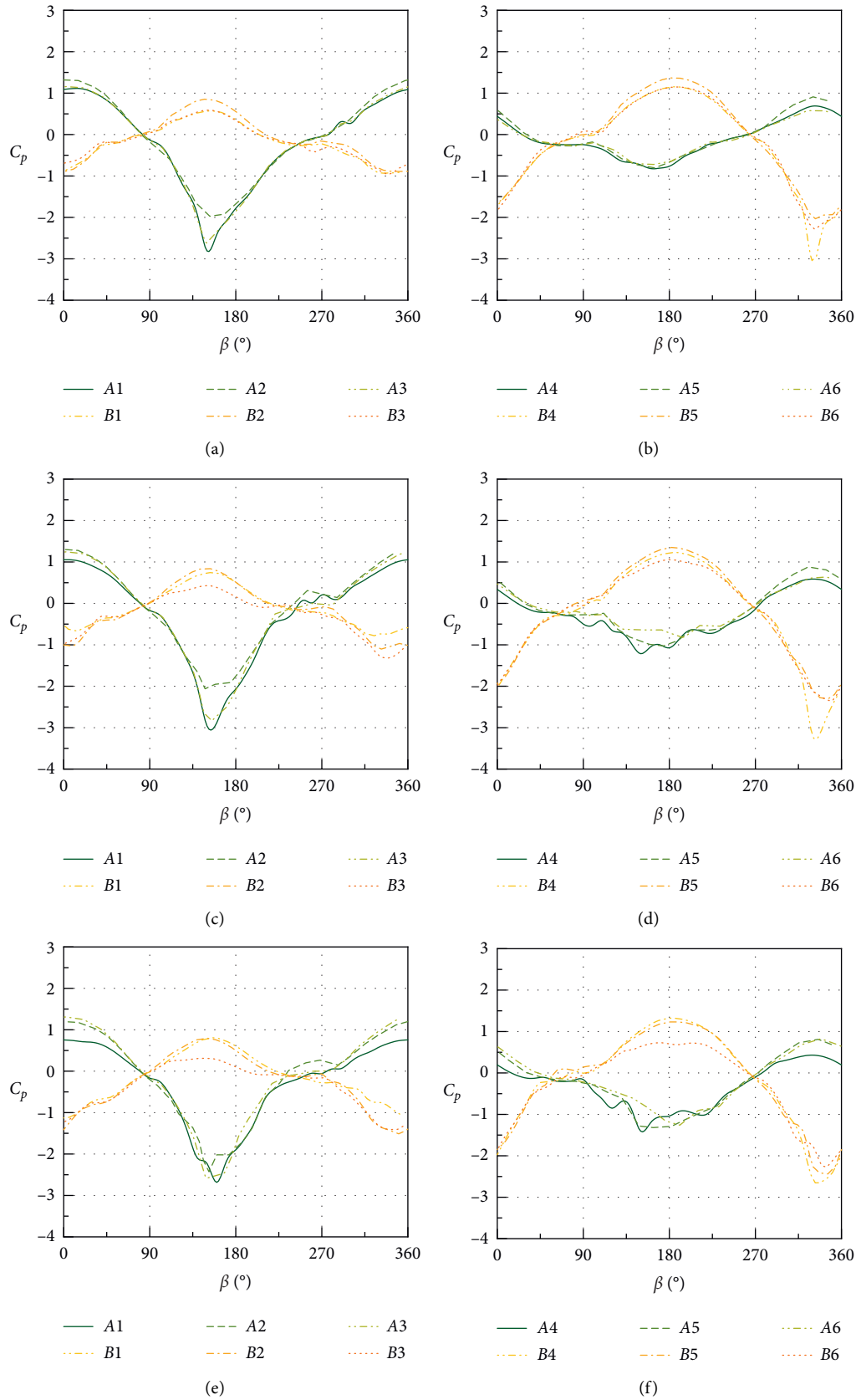

Figure 10: Continued.

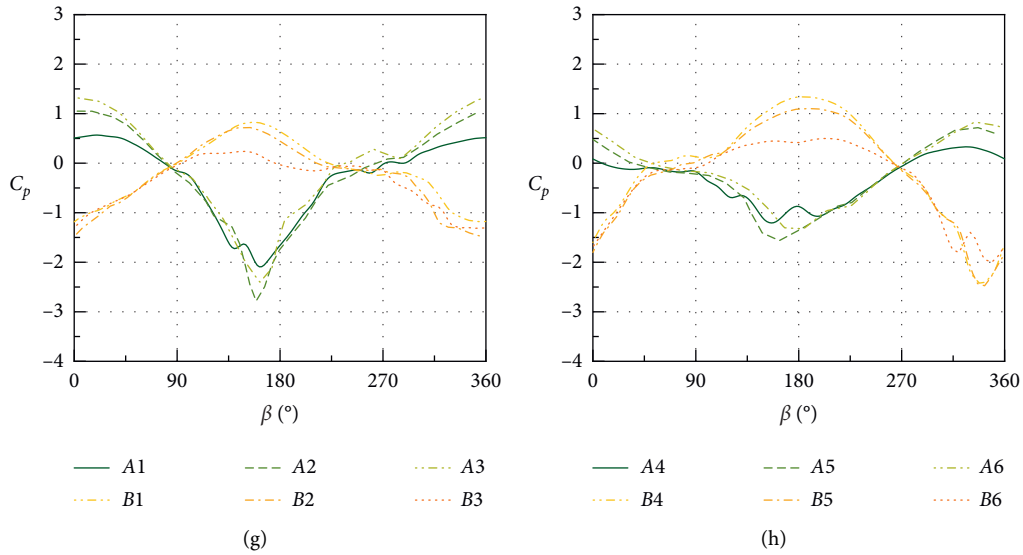

Figure 10: Wind pressure coefficient of the monitoring point on the antenna surface changes with respect to the elevation angle, $\alpha = 0$–30°, $\beta = 0$–360°. (a) $\alpha = 0^\circ$. (b) $\alpha = 0^\circ$. (c) $\alpha = 10^\circ$. (d) $\alpha = 10^\circ$. (e) $\alpha = 20^\circ$. (f) $\alpha = 20^\circ$. (g) $\alpha = 30^\circ$. (h) $\alpha = 30^\circ$.

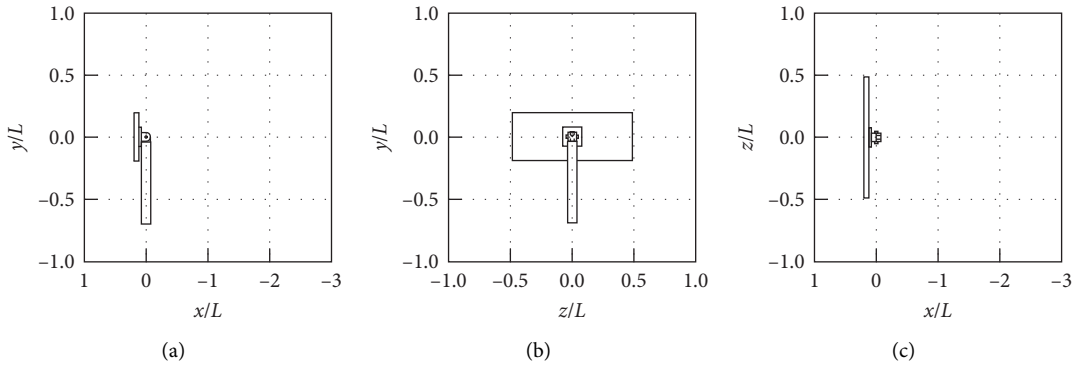

Figure 11: Definition of three views of antenna. (a) Side view. (b) Rear view. (c) Top view.

points with respect to the azimuth angle. Figure 9 shows the positions of the wind pressure coefficient monitoring points distributed on the front and rear sides of the antenna. Six monitoring points are arranged on the front and rear of the antenna, respectively, where A is the front of the antenna, and B is the back of the antenna. Figure 10 shows the wind pressure coefficient variation at the monitoring point on the antenna surface with respect to the elevation angle. As β increases from 0° to 360°, for the front of the antenna, the wind pressure coefficient at monitoring points $A1$, $A2$, and $A3$ first decreases rapidly and then increases rapidly relative to the increase in azimuth angle, and the minimum value appears near $\beta = 150^\circ$. For the rear of the antenna, the wind pressure coefficient at $B5$, $B6$, and $B7$ first increases with respect to the azimuth angle and then decreases rapidly, and the minimum value appears near $\beta = 330^\circ$. With an increase in the elevation angle, the positive peak values of wind pressure coefficient at $B3$ and $B6$ around the lower edge of the antenna decrease significantly, while the positive peak values of wind pressure coefficient at $B1$, $B2$, $B4$, and $B5$ change little. The negative peaks of the wind pressure coefficient at the monitoring points $A2$ and $A5$ in the middle of the antenna gradually decrease, the negative peak values of the wind pressure coefficient at $A1$ and $A3$ on the front of the antenna gradually increase, and the negative peak values of the wind pressure coefficients at $A4$ and $A6$ decrease. It shows that as the elevation angle increases, the positive pressure concentration area of the antenna is moving to the upper edge.

When $\alpha = 0^\circ$, the wind pressure coefficients at monitoring points 1 and 3, as well as points 4 and 6, are highly correlated with the change in azimuth angle. When $\beta = 150^\circ$, the difference in wind pressure coefficients between the front and rear side of monitoring points 1, 2, and 3 is the largest; when $\beta = 330^\circ$, the difference of wind pressure coefficients between the front and rear side of monitoring points 4, 5, and 6 is the largest. When $\alpha = 10^\circ$, the wind pressure coefficient at monitoring point 1 and point 3 has similar changes with respect to the azimuth angle. Due to the increase in the elevation angle, the wind pressure coefficient at

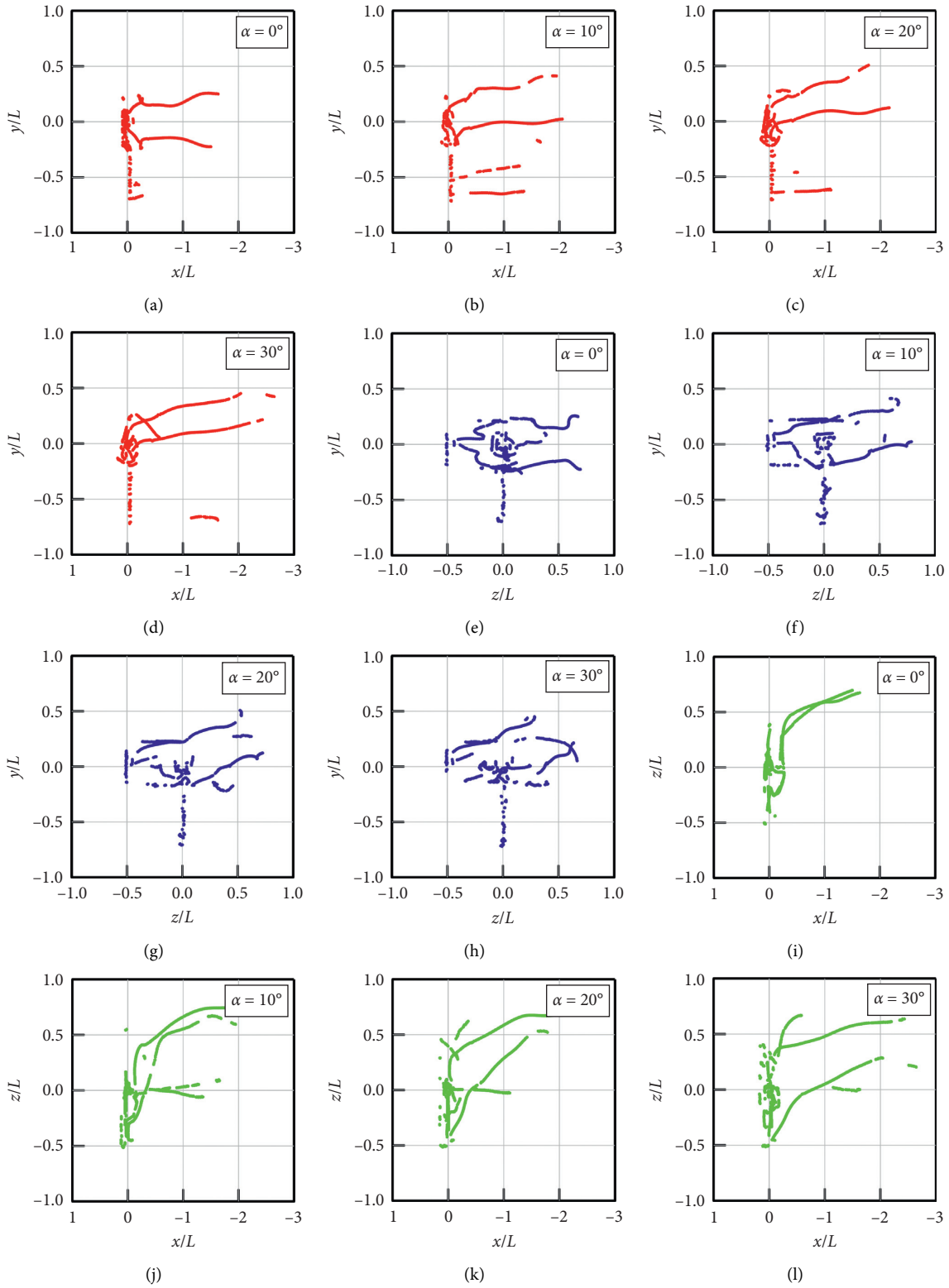

FIGURE 12: The distribution of the vortex core trajectory with respect to the elevation angle in three views, $\alpha = 0$–30°, $\Delta = 10^{\circ}$, $\beta = 0^{\circ}$, $K = 0.4$. (a–d) Side view; (e–h) rear view; (i–l): Top view.

the front monitoring point fluctuates with respect to the azimuth angle. Besides, when $\beta = 155^{\circ}$, the difference of wind pressure coefficients between the front and rear side of monitoring points 1, 2, and 3 is the largest, especially near $\beta = 330^{\circ}$. The difference in wind pressure coefficients on the front and rear side of monitoring points 4, 5, and 6 reached

the maximum. When $\alpha = 20–30^{\circ}$, the wind pressure coefficient of each monitoring point fluctuates with respect to the azimuth, and the correlation of the wind pressure coefficient at each monitoring point decreases. When $\beta = 160^{\circ}$, the difference in wind pressure coefficients at monitoring points 1, 2, and 3 is the largest; when $\beta = 335^{\circ}$, the difference in wind pressure coefficients at monitoring points 4, 5, and 6 is the largest.

As the antenna rotates, increasing the elevation angle will decrease the positive peaks of the wind pressure coefficient around the lower edge of the back of the antenna and reduce the negative pressure value of the monitoring point around the middle of the front of the antenna. When $\alpha = 0^{\circ}$ and $\beta = 0^{\circ}$, the wind pressure coefficients for $A1–A3$ are almost the same. As the elevation angle increases, the wind pressure coefficient for $A1$ at $\beta = 0^{\circ}$ decreases significantly. Note that the wind pressure coefficient at $B1–B6$ on the back of the antenna is more sensitive to the change of elevation angle. With an increase in the elevation angle, the azimuth angle, at which the maximum difference between the wind pressure coefficients at the front and rear of the antenna corresponding to the monitoring point appears, is almost unchanged, that is, $\beta = 155^{\circ}$. Although the mean, maximum, root mean square value of aerodynamic coefficient may increase with an increase in the antenna elevation angle, it can significantly reduce the wind pressure coefficient around the middle of the front of the antenna and the lower edge of the back, as shown in curves B3 and B6 in Figure 10.

4.2. The Vortex Core Trajectory around the Antenna Changes with Respect to the Elevation Angle. The wind pressure coefficient depends on the separation position of the airflow separation and vortex shedding. The existence of both affects the symmetrical distribution of the pressure coefficient. The position of severe vortex impact will lead to the failure of antenna structure due to fatigue load; for the antenna with azimuthal rotation, the surface pressure distribution is greatly affected by the vortex core distribution [22, 25, 26]. The pressure at the vortex core is negative, and the pressure on the antenna surface is proportional to the distance of the vortex core. The smaller the distance, the lower the pressure value. To further investigate the mechanism of the influence of unsteady flow on the pressure distribution on the antenna surface at different elevation angles, Figure 11 shows the position of the antenna in three views when $\alpha = 0^{\circ}$ and $\beta = 0^{\circ}$, respectively. When $\alpha = 10^{\circ}$, 20°, and 30°, the antenna position does not change, but the elevation angle changes. Figure 12 shows the vortex core trajectory distribution with respect to the elevation angle change in the three views.

From the side view, when the elevation angle of the antenna increases, the two vortex core trajectories generated by the vortex shedding from the upper and lower edges are moving in the positive direction of the y-axis, and the distance between the vortex core trajectories is reduced, and the vortex core trajectory drawn from the upper edge is further than the antenna surface distance. In addition, with an increase in elevation angle, the track of the vortex core around the antenna becomes short and discontinuous.

From the rear view, the vortex core distribution around the left and right edges of the antenna is asymmetric, and the distribution of the vortex core trajectory in the negative direction of the z-axis is short and denser than the other side. As the elevation angle increases, the asymmetry of the left and right vortex core distribution decreases, and the asymmetry of the vortex core distribution on the upper and lower sides increases.

From the top view, when $\alpha = 0^{\circ}$, the upper and lower edge shedding vortices propagate downstream simultaneously, and the vortex core trajectory around the antenna is continuous and concentrated. After the elevation angle increases, the vortex core trajectories become short and dispersed, while the upper edge vortex sheds early and starts to propagate rapidly downstream, and the distance between them in the x-axis increases.

Figure 12 shows that when $\alpha = 0^{\circ}$, the vortex core trajectory is mainly distributed in the rear side of the antenna, and the distance between the shedding vortices generated at the upper and lower edges and the antenna surface is the same. Compared with other elevation angles, the drag coefficient is the largest, as shown in Figure 5(i). When $\alpha = 10^{\circ}$, most of the vortex core is in the z-axis forward region, but there is a certain distance from the antenna surface, which has little effect on the pressure distribution on the antenna surface. The vortex core located in the negative region of the z-axis is continuous and close to the antenna surface, while the vortex core trajectories at other elevation angles are far away from the antenna, scattered, and discontinuous. When $\beta = 0^{\circ}$, the lateral force coefficient is the smallest among all elevation angles, and the azimuth moment coefficient is the largest among all elevation angles, as shown in Figure 5(g). When $\alpha = 20^{\circ}$, the shedding vortices at the upper and lower edges of the antenna move towards the negative direction of the x-axis and the positive direction of the y-axis, and the vortex cores are continuous and primarily distributed in the positive direction of the y-axis. In addition, the edge shedding vortices at the upper and lower edges are closer to the antenna surface than that at $\alpha = 0^{\circ}$. The pitching moment coefficient for the antenna at $\alpha = 20^{\circ}$ and $\beta = 0^{\circ}$ is the largest among all elevation angles, as shown in Figure 5(l). When $\alpha = 30^{\circ}$, the vortex core trajectories distributed directly behind the antenna are mostly scattered and discontinuous. The vortex core trajectories generated by the upper edge are significantly farther from the antenna surface than other elevation angles, and the vortex core has less influence on the pressure distribution on the antenna surface. Therefore, the pitching moment coefficient for the antenna at $\beta = 0^{\circ}$ is the smallest, as shown in Figure 5(l).

5. Conclusions

Based on dynamic force testing in a wind tunnel, a flat plate antenna was tested at a range of elevation angles and reduced frequencies. Four elevation angles ($\alpha = 0^{\circ}$, 10°, 20°, 30°) of the antenna at three reduced frequencies ($K = 0.2, 0.24, 0.4$) were selected for comparison. The variation curves of the aerodynamic coefficients with respect to the azimuth angle under the influence of elevation angle and reduced frequency in a

rotation period were given, focusing on the mean, maximum, and root mean square value of the aerodynamic coefficients with respect to elevation angle and reduced frequency. A comparison of the numerical simulation results for the aerodynamic coefficients at different antenna elevation angles shows that the two sets of results are in good agreement, indicating the possibility of using numerical simulations to obtain the unsteady aerodynamic characteristics of the antenna, and the influence mechanism, whereby the unsteady flow field structure on the aerodynamic characteristics of the antenna is also briefly introduced. The conclusions are as follows.

When the antenna rotates at the same reduced frequency, the changes in the peak or peak-to-peak values of the aerodynamic coefficients relative to the elevation angle are not monotonic; that is, increasing the elevation angle does not necessarily reduce the aerodynamic coefficient peak of the peak-to-peak value. The mean, maximum, and root mean square values of the aerodynamic coefficients increase monotonically with respect to the elevation angle. At different reduced frequencies, the peak-to-peak values of C_x, C_z, and C_{my} are the smallest at $\alpha = 30^{\circ}$, which shows that, compared to the reduced frequency, a large elevation angle can reduce the peak-to-peak value of the aerodynamic coefficient to a certain extent.

Therefore, the aerodynamic coefficient is affected by the elevation angle and the reduced frequency. Note that, in the range of $\alpha = 0$–30°, when the elevation angle is large, the mean, maximum, and root mean square value of the aerodynamic coefficients are significantly reduced relative to the increase in elevation angle. Therefore, when the antenna elevation adjustment range is allowed, the antenna should be prevented from rotating under a slight elevation angle to avoid large fluctuations in wind load and ensure the wind resistance performance of the antenna.

As the elevation angle increases, there is almost no change in the position of the greatest difference in wind pressure coefficients between the front and rear of the antenna corresponding to the monitoring point, that is, near $ß = 155^{\circ}$. In a small range of antenna elevation angles, it is possible to increase the mean, maximum, and root mean square values of the aerodynamic coefficients by increasing the elevation angle, but this significantly reduces the wind pressure coefficient around the middle of the front and the lower edge of the back of the antenna. This is because as the elevation angle of the antenna increases, the asymmetry of the left and right distribution of the vortex core near the antenna weakens, while the asymmetry of the vertical distribution increases.

Data Availability

The data used to support the findings of this study are available from the corresponding author upon request.

Conflicts of Interest

The authors declare that there are no conflicts of interest regarding the publication of this paper.

Acknowledgments

This work was supported by the Priority Academic Program Development of Jiangsu Higher Education Institutions (PAPD).

References

[1] M. Mohammadi Shirkolaei and J. Ghalibafan, "Scannable leaky-wave antenna based on ferrite-blade waveguide operated below the cutoff frequency," *IEEE Transactions on Magnetics*, vol. 57, no. 4, pp. 1–10, 2021.

[2] W. Gawronski, *Modeling and Control of Antennas and Telescopes*, Springer, Berlin, Germany, 2008.

[3] R. B. Blaylock Jr., B. Dayman, and N. L. Dayman, "Wind tunnel testing of antenna models*," *Annals of the New York Academy of Sciences*, vol. 116, no. 1, pp. 239–274, 1964.

[4] N. L. Fox, *Experimental Data on Wind-Induced Vibrations of a Paraboloidal Reflector Antenna Model, Report No. NASA-CR-57422, JPL-CP-5; Jet Propulsion Lab*, California Institute of Technology, Pasadena, CA, United States, 1963.

[5] J. Y. R. Bicknell, *Air Loads and Pressure Distribution on a Parabolic Antenna Model*, 1962.

[6] J. D. Holmes, *Wind Loading of Structures*, CRC Press, London, UK, 3rd edition, 2017.

[7] L. Lu-Jun, L. Zhong-Xuan, and W. Fan, "Research on structure design of long strip radar antenna," *Electro-Mechanical Engineering*, vol. 35, pp. 21–27, 2019.

[8] G. A. O. Yan-long, D. U. Ping-an, and D. U. Qiang, "Simulation and analysis of the blockage ratio for antenna wind tunnel test," *Modern Radar*, vol. 32, pp. 79–83, 2010.

[9] M. Kron, "Load distribution on the surface of paraboloidal reflector antennas," *Deep Space Network Progress Report*, vol. 5, pp. 122–128, 1971.

[10] W. K. Gawronski and J. A. Mellstrom, *Field Verification of the Wind Tunnel Coefficients. The Telecommunications and Data Acquisition Report*, Report No. 42-119, Jet Propulsion Laboratory; California Institute of Technology, Pasadena, CA, United States, 1994.

[11] P. Sachs, *Wind Forces in Engineering*, Pergamon Press, Oxford, UK, 2nd edition, 1978.

[12] G. Lombardi, "Wind-tunnel tests on a model antenna rotating in a cross flow," *Engineering Structures*, vol. 13, no. 4, pp. 345–350, 1991.

[13] S. Muggiasca, F. Ripamonti, D. Rocchi, and A. Zasso, *Numerical and Experimental Investigation on a Maritime Radar Scanner*, Fluid Structure Interaction, Crete, Greece, 2009.

[14] B. Gumusel, C. Camci, and C. Camci, "Aerodynamic drag characteristics and shape design of a radar antenna used for airport ground traffic control," *Progress in Computational Fluid Dynamics, An International Journal*, vol. 10, no. 1, pp. 32–39, 2010.

[15] L. L. Trimmer and E. L. Clark, *Transformation of Axes Systems by Matrix Methods and Application to Wind Tunnel Data Reduction*, Report No. AEDC TDR 63–224, Arnold Engineering Development Center, United States Air Force, Ohio, OH, USA, 1963.

[16] M. Shields and K. Mohseni, "Static and dynamic lateral loads for a low aspect ratio wing at low Reynolds numbers," in *Proceedings of the 30th AIAA Applied Aerodynamics Conference*, New Orleans, LA, USA, June 2012.

[17] X. Xia and K. Mohseni, "Lift evaluation of a two-dimensional pitching flat plate," *Physics of Fluids*, vol. 25, no. 9, p. 91901, 2013.

[18] F. R. Menter, "Two-equation eddy-viscosity turbulence models for engineering applications," *AIAA Journal*, vol. 32, no. 8, pp. 1598–1605, 1994.

[19] M. Strelets, *Detached Eddy Simulation of Massively Separated Flows*, AIAA Journal, Reno, NV, USA, 2001.

[20] J. Wang, P. Van Phuc, Q. Yang, and Y. Tamura, "LES study of wind pressure and flow characteristics of flat-roof-mounted solar arrays," *Journal of Wind Engineering and Industrial Aerodynamics*, vol. 198, no. 2020, Article ID 104096, 2020.

[21] D. J. Garmann, M. R. Visbal, and P. D. Orkwis, "Three-dimensional flow structure and aerodynamic loading on a revolving wing," *Physics of Fluids*, vol. 25, no. 3, pp. 3439–3448, 2013.

[22] Q. Zhang and Y. Liu, "Separated flow over blunt plates with different chord-to-thickness ratios: unsteady behaviors and wall-pressure fluctuations," *Experimental Thermal and Fluid Science*, vol. 84, pp. 199–216, 2017.

[23] A. Scarabino, M. G. Sainz, F. Bacchi, J. S. Delnero, and A. Canchero, "Numerical and experimental study of unsteady wind loads on panels of a radar aerial," *Wind and Structures*, vol. 23, no. 1, pp. 1–18, 2016.

[24] B. Wu, S. Li, S. Cao, Q. Yang, and L. Zhang, "Numerical investigation of the separated and reattaching flow over a 5:1 rectangular cylinder in streamwise sinusoidal flow," *Journal of Wind Engineering and Industrial Aerodynamics*, vol. 198, Article ID 104120, 2020.

[25] T. Li, Q. Yang, and T. Ishihara, "Unsteady aerodynamic characteristics of long-span roofs under forced excitation," *Journal of Wind Engineering and Industrial Aerodynamics*, vol. 181, pp. 46–60, 2018.

[26] D. Rockwell, "VORTEX-BODY interactions," *Annual Review of Fluid Mechanics*, vol. 30, no. 1, pp. 199–229, 1998.